Materials Today Bio 29 (2024) 101345

Contents lists available at ScienceDirect

Materials Today Bio

journal homepage: www.journals.elsevier.com/materials-today-bio

Highly stable and near-infrared responsive phase change materials for targeted enzyme delivery toward cancer therapy

Yuqiong Xia [a,b,*], Chang Liu [a], Xuejuan Zhao [a], Keyun Wu [a], Jianxia Cao [a], Yutian Cao [a,b], Cheng Zhu [c,**], Xianghan Zhang [a,b,***]

[a] Engineering Research Center of Molecular- and Neuro-imaging of Ministry of Education, School of Life Science and Technology, Xidian University, Xi'an, Shaanxi, 710126, China

[b] Guangzhou Institute of Technology, Xidian University, Guangzhou, Guangdong, 510555, China

[c] Tianjin Key Laboratory of Function and Application of Biological Macromolecular Structures, School of Life Sciences, Tianjin University, 92 Weijin Road, Nankai District, Tianjin, 300072, China

ARTICLE INFO

Keywords:
Phase change material
Enzyme dynamic therapy
Enzyme delivery
Near infrared responsive

ABSTRACT

Natural enzyme-based catalytic cascades have garnered increasing attention in cancer therapy, but their clinical utility is greatly limited due to loss of function during *in vivo* delivery. Here, we developed an enzyme delivering nanoplatform (GCI@RPCM) with great *in vivo* stability and achieve NIR-triggered enzyme dynamic therapy. This nanoplatform is created with encapsulation of nature enzymes (glucose oxidase and chloroperoxidase) and photothermal agent (indocyanine green) within tumor targeting and thermo-responsive phase change materials (RPCMs). With NIR irradiation for 10 min, GCI@RPCM can release 41 % of the enzymes and generate abundant reactive oxygen species (ROS), which showed significant tumor cell inhibition. After intravenous injection, GCI@RPCM can efficiently accumulate at the tumor site and local NIR treatment resulted in complete tumor eradication without detectable systemic toxicity. This study provides a highly stable and NIR-controllable smart delivery system and achieve enzyme dynamic therapy for enhanced breast cancer therapy.

1. Introduction

With a total of 19.3 million new cases and 9.9 million deaths occurred in 2020, cancer remained a major global health problem [1]. As an alternative to traditional therapeutic modalities such as chemotherapy and radiotherapy, enzyme dynamic therapy (EDT), in which chloroperoxidase (CPO) catalyzes chloride with hydrogen peroxide (H_2O_2) to generate hypochloric acid (HClO) and form singlet oxygen ($^1O_2$), offering new opportunities to combat tumor [2,3]. However, the instability of chloroperoxidase in body fluids greatly restricts the application of EDT in tumor therapy, underscoring the need for highly stable enzyme delivery systems. Although nanocarriers such as polymers [4,5], liposomes [6–10] and metal-organic frameworks [11] have greatly improved the therapeutic efficacy of enzymes, these carriers still have premature enzyme release, causing potential side effects in normal organs and tissues. Therefore, enzyme delivering systems with high stability are highly required to achieve efficient and safe use of EDT.

Recently, phase change materials (PCMs), with reasonable melting point, low cost, good chemical stability and great biocompatibility, have received considerable interest in acting as gating materials and stimuli-responsive materials for cancer therapy [12,13]. Combing thermo-responsive PCMs [14] and near-infrared (NIR) photothermal agents [15–21] would obtain NIR-responsive PCMs, which can precisely target tumor by controlling irradiation range and reserve the high stability of PCMs, thereby avoiding or minimizing potential harm to normal organs and tissues [22–24]. NIR-responsive PCMs have been developed to deliver small molecular drugs [25–27] and seal nanoparticles [28] but have never been used to deliver natural enzymes. It is not clear whether

* Corresponding author. Engineering Research Center of Molecular- and Neuro-imaging of Ministry of Education, School of Life Science and Technology, Xidian University, Xi'an, Shaanxi, 710126, China.

** Corresponding author. Tianjin Key Laboratory of Function and Application of Biological Macromolecular Structures, School of Life Sciences, Tianjin University, 92 Weijin Road, Nankai District, Tianjin, 300072, China.

*** Corresponding author. Engineering Research Center of Molecular- and Neuro-imaging of Ministry of Education, School of Life Science and Technology, Xidian University, Xi'an, Shaanxi, 710126, China.

E-mail addresses: yqxia@xidian.edu.cn (Y. Xia), cheng_zhu@tju.edu.cn (C. Zhu), xhzhang@xidian.edu.cn (X. Zhang).

https://doi.org/10.1016/j.mtbio.2024.101345
Received 13 August 2024; Received in revised form 7 November 2024; Accepted 15 November 2024
Available online 19 November 2024

proteins (natural enzymes) and PCMs have strong interaction. Considering the hydrophobic domains in the enzymes, we hypothesized that the enzymes could bind to the PCMs through hydrophobic interaction and NIR-responsive PCMs could be utilized to deliver enzymes for precise cancer therapy.

Herein, we report super-stable and NIR-responsive PCMs (GCI@RPCMs) for targeted enzyme delivery toward cancer therapy. The GCI@RPCMs consist of arginylglycylaspartic acid (RGD) ligand-modified PCMs as the tumor-targeting and thermo-responsive carrier [29], indocyanine green (ICG) as the NIR photothermal agent [30], glucose oxidase (GOx) [31,32] and chloroperoxidase (CPO) [33] as enzyme cascades [34]. The formation of the GCI@RPCMs and their working mechanism at the tumor site after intravenous injection are illustrated in Scheme 1. This design allows for the super-stable encapsulation of enzyme cascades at 37 °C during circulation but enables rapid release in the tumor tissue upon NIR irradiation, which facilitated tumor-specific enzyme delivery, enhancing antitumor efficacy and reducing side effect. Thus, our work offers a super-stable and NIR light responsive enzyme carrier for EDT as well as other highly potent protein therapies.

2. Materials and methods

2.1. Synthesis and characterization of phase-change materials

The GCI@RPCMs (GOx/CPO/ICG/RGD/PCMs) were prepared with nanoprecipitation method. In detail, PCM solution (mixture of lauric acid and stearic acid in methanol, 3.5:1, mass ratio, 4 mg/mL, 2 mL), ICG solution (5 mg/mL in DMF, 1 mL), GOx solution (5 mg/mL in water, 0.5 mL) and CPO solution (300 units/mL in water, 187.5 μL) were added dropwise into preheated mixture of lipid solution (3.75 mg EPC, 1.25 mg DSPE-PEG2000 and 0.31 mg DSPE-RGD, in 4 % aqueous ethanol solution) at 50 °C, followed by vigorous vortex for 10 min. Then, the mixed solution was cooled in an ice-water bath for 10 min, followed by being heated to ambient temperature and vortexed vigorously for 10 min. Subsequently, the mixture was filtered through a 0.2 μm cellulose acetate membrane (Merck Millipore). Finally, the homogenized PCMs underwent dialysis (MWCO 300K) in water for three times to remove the unencapsulated proteins.

The GCI@PCMs were prepared similarly to GCI@RPCMs, except that DSPE-RGD was not included. The GI@PCMs, CI@PCMs and (I@PCMs were prepared similarly to GCI@PCMs, except that CPO, GOx and GOx/CPO were not added, respectively.

The hydrodynamic diameter and zeta potentials of different PCMs were measured with dynamic light scattering (DLS; Malvern ZEN3690). The stability of PCMs was evaluated by monitoring the changes in hydrodynamic diameters of GCI@RPCM in water, PBS and 10 % FBS (10 % FBS mixed with 90 % PBS) for seven days.

The encapsulation efficiency (EE) and loading content (LC) of ICG were quantitated by NIR absorption at 785 nm (LAMBDA650, PerkinElmer, USA) after destroying PCMs by methanol. The EE of ICG is defined by the concentration of the ICG detected in the PCMs over the initial concentration used to make the formulation. The LC is defined as the concentration of ICG to that of lipids in the PCMs (w/w). The EE and LC of GOx and CPO were quantitated by the Bradford protein assay after destroying PCMs with methanol.

The NIR absorption spectra of free ICG and different PCMs (I@PCMs, CI@PCMs, GI@PCMs, GCI@PCMs, GCI@RPCMs) in water (ICG

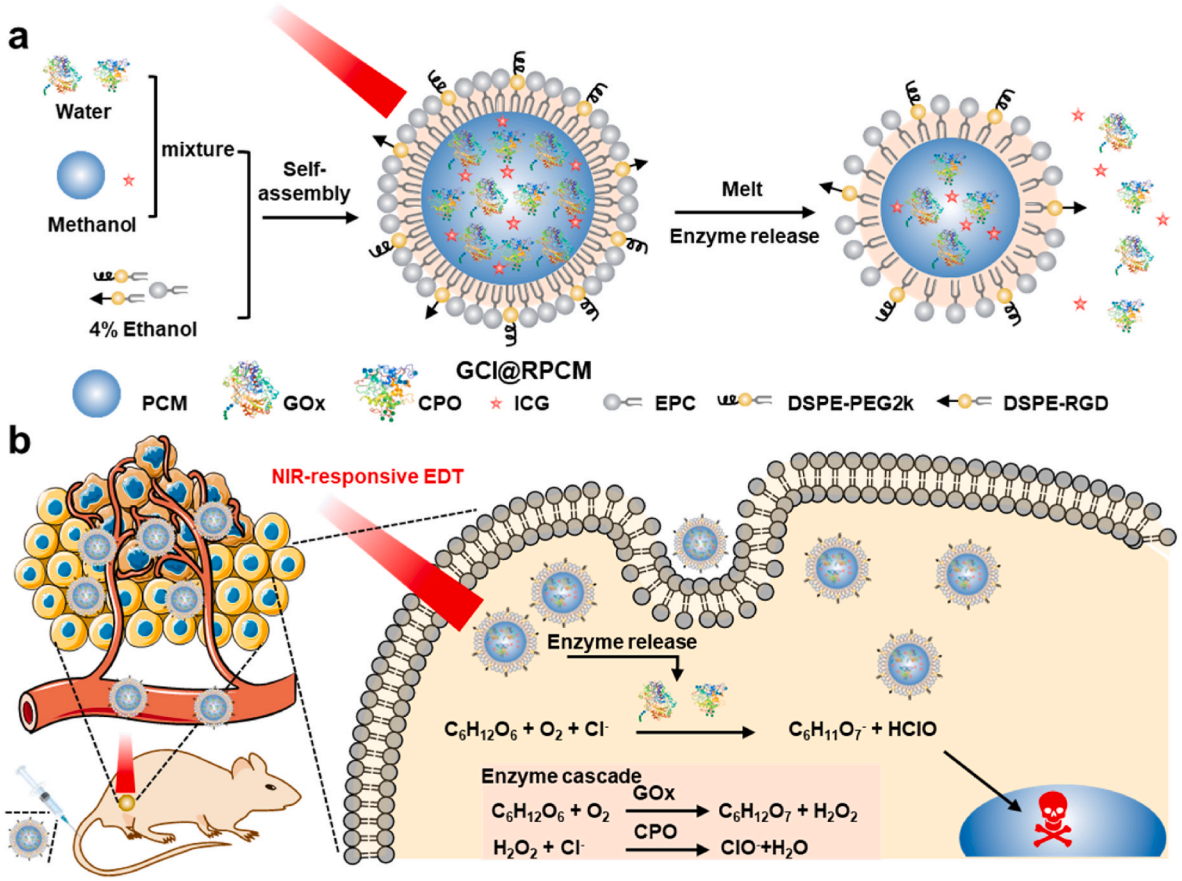

Scheme 1. (a) Schematic illustration of the preparation of GCI@RPCMs consisting of PCMs, two natural enzymes, GOx, and CPO, photothermal agent ICG and RGD modification via a nanoprecipitation method. Upon irradiation, GCI@RPCMs melt and release enzymes. (b) The NIR-responsive enzyme dynamic therapy (EDT) against breast cancer models.

concentration: 2.5 μg/mL) was measured in the range of 400–900 nm (LAMBDA650, PerkinElmer, USA).

The fluorescence spectra of free ICG and different PCMs (I@PCMs, CI@PCMs, GI@PCMs, GCI@PCMs, GCI@RPCMs) in water (ICG concentration: 10 μg/mL) were measured on a fluorescence spectrometer (FLS1000, Edinburgh, UK) with excitation at 765 nm, and the emission was collected from 780 to 900 nm.

2.2. In vitro photothermal measurement

The temperature profiles of free ICG and GCI@RPCMs in water (ICG concentration: 0, 2.5, 5, 10, 20 μg/mL) during irradiation with NIR laser were determined by a thermal imager (A300, FLIR). Briefly, 0.1 mL (each) of water, free ICG, or GCI@RPCMs was irradiated using a NIR laser (808 nm, 1 W/cm^2 or 1.5 W/cm^2), and the temperature of each sample was monitored for 5 min.

2.3. NIR laser triggered morphology change measurement

The morphology of GCI@RPCMs before and after NIR irradiation (808 nm, 1.4 W/cm^2, 10 min) was measured with TEM imaging (Talos F200X) operated at an acceleration voltage of 200 kV. For sample preparation, 10 μL of GCI@RPCM (containing 0.1 mg/mL lipids) were dropped onto a 200/300 mesh F/C copper TEM grid (Suzhou Crystal Silicon Electronics & Technology Co., Ltd., Suzhou, China), and the excess dispersion was then removed after 1 h; after that, the adsorbed sample was stained with 10 μL of 3 % phosphotungstic acid for 30 s.

2.4. In vitro release kinetics measurement

To quantify the *in vitro* release kinetics of GOx/CPO from GCI@RPCMs, GOx/CPO were first labeled with FITC (named FITC-GC). FITC-GC was synthesized by crosslinking GOx/CPO with 5-FITC according to a reported protocol [35]. The protein concentration of FITC-GC was calculated according to the following formula: GC (mg/mL) = [A_{280}-0.31 × A_{495}]/1.4, where A_{280} and A_{495} were the UV–vis absorbances of GC solution at 280 nm and 495 nm. Then, FITC-GCI@RPCMs were synthesized similarly to that of GCI@RPCMs except that GOx and CPO was replaced with FITC-GC (1 mL, 0.54 mg/mL in water).

To monitor the release kinetics of FITC-GC under NIR irradiation, the FITC-GCI@RPCMs (1 mL, [ICG] = 20.0 μg mL^{-1}) in water was irradiated by the 808 nm NIR laser at a laser fluence of 0.8 W cm^{-2} for 10 min. At indicated time points (0, 2, 4, 6, 8 and 10 min), the irradiated solution (10 μL) was retrieved and mixed with water (90 μL) for fluorescence measurements using a microplate reader (Ex = 490 nm, Em = 500–550 nm). The release percentage of FITC-GC was calculated by (I_t-I_0)/(I_{100}-I_0), where I_t is the fluorescence intensity of the solution at the indicated time point, I_0 is the initial fluorescence intensity of the solution before laser irradiation, and I_{100} is the fluorescence intensity of FITC-GCI@RPCM ([ICG] = 20.0 μg mL^{-1}, 10 μL) mixed with methanol (90 μL). The release kinetics of FITC-GC without NIR irradiation at pH = 3, 5, 7 was performed similarly.

2.5. Enzymatic activity measurement

Thermo-responsive enzymatic Activity was measured through evaluating the generation of HClO with dye decolorization at different temperatures (25 °C, 37 °C and 45 °C). In detail, 50 μL of free GOx/CPO or GC@PCM (GOx concentration: 0, 1, 3, 5, 7 and 9 μg/mL; CPO concentration: 0, 22.5, 67.5, 112.5, 157.5 and 202.5 mU/mL) was incubated with the substrate solution in air atmosphere at different temperatures for 12 h. In a typical experiment, the substrate solution is a mixture of glucose solution (1 mg/mL, 1 mL), NaCl solution (2 M, 2 μL), Na_2PO_4 buffer solution (1 M, 5 μL) and AO7 solution (1 mg/mL, 10 μL). At the end of the enzymatic reaction, the UV–vis absorption of the reaction solutions in the range of 350–600 nm was measured (LAMBDA650, PerkinElmer, USA). The decolorization efficiency (η) of AO7 dye after different treatments was calculated as follows: η = (A_0-A_d)/A_0 × 100 %, where A_d was the absorbance of the substrate at 485 nm after treatment with free GOx/CPO or GC@PCM and A_0 was the absorbance of the substrate solution at 485 nm. At 45 °C, the enzyme activity of GOx/CPO at pH = 3, 5, 7 and single GOx or CPO at neutral conditions was evaluated similarly. For Michaelis-Menten constant determination, the enzyme activity of free GOx/CPO or GC@PCM nanoparticles at 45 °C with different substrate concentrations (1–10 mg/mL) were measured. The velocity was determined by reduced absorbance divided by time (12 h). The values of the Michaelis-Menten constant (K_m) were determined from Michaelis-Menten equation.

2.6. Cell culture

Murine breast cancer cells (4T1) and human breast endothelial cells (MCF-10A) were obtained from American Type Culture Collection (ATCC). 4T1 cells were cultured in RPMI-1640 medium (Gibco) supplemented with 10 % FBS (Gibco) and 1 % penicillin and streptomycin (P/S, HyClone). The cultures were maintained in an incubator at 37 °C in a humidified atmosphere containing 5 % CO_2, and the medium was changed every other day. The subculture of MCF-10A cells (breast epithelial cells) was similar to that of 4T1 cells, except that the medium was DMEM (Gibco) supplemented with 10 % FBS and 1 % P/S.

2.7. Cellular uptake of PCMs

TPE-BICOOH@PCM and TPE-BICOOH@RPCMs containing aggregation-induced emission dyes (TPE-BICOOH) were used to quantify the cellular uptake of PCMs. TPE-BICOOH was synthesized as previously reported [36]. TPE-BICOOH@PCM and TPE-BICOOH@RPCMs were synthesized similar to I@PCM and I@RPCMs, except that ICG was replaced with TPE-BICOOH (32.2 μL, 2 mg/mL in DMSO).

To monitor the cellular uptake of TPE-BICOOH@PCMs and TPE-BICOOH@RPCMs in 4T1 cells, the cells in 96-well plates were treated with TPE-BICOOH@PCMs or TPE-BICOOH@RPCMs (TPE-BICOOH 5 μM, 100 μL/well) for different time (2, 4, 8, 12 h). After that, the cells were washed with PBS and imaged with fluorescence microscopy (Leica, Cy5 channel). The mean fluorescence intensity of cells was analyzed with Image J. To prove the enhanced uptake of TPE-BICOOH@RPCMs was due to arginylglycylaspartic acid (RGD) ligand-mediated targeting, the 4T1 cells were pre-treated with free RGD peptides for 3 h and then incubated with TPE@RPCMs for 2 h. To evaluate the tumor cell specificity of TPE-BICOOH@RPCMs, the uptake of TPE-BICOOH@PCMs and TPE-BICOOH@RPCMs in MCF-10A cells after incubation for different time (2, 4, 8 and 12 h) was also investigated.

2.8. Cytotoxicity

To quantify the cytotoxicity of PCMs with laser irradiation, 4T1 cells were treated with PCMs (ICG concentration: 10, 15, 20 μg/mL) in cell media supplemented with 20 mM NaCl for 20 h. For enzyme cascade reaction, the glucose was 2000 mg/L, the Cl^- was 128 mM (400 mg/L or 5 mM KCl and 6000 mg/L or 103 mM NaCl in the commercial cell media as well as supplemented 20 mM NaCl) in the cell media and the oxygen in the cell incubator was about 20 %. Then, the media were replaced with fresh media and followed by laser irradiation (808 nm, 1.5 W/cm^2, 5 min). Later, the cells were further incubated for 4 h before MTT assay. To evaluate the cytotoxicity of PCMs without laser irradiation, 4T1 cells were treated with PCMs (ICG: 10, 15, 20 μg/mL) in cell media supplemented with 20 mM NaCl for 24 h. The cell viability was determined by the MTT assay similar to our previous work [7].

To visualize the cytotoxicity of PCMs with or without laser treatment, 4T1 cells in 24-well plates were first incubated with different PCMs (ICG: 20 μg/mL) for 24 h with or without laser irradiation (808

nm, 1.5 W/cm^2, 5 min) and then collected and stained with Calcein-AM/PI Double Stain Kit, followed by observation under fluorescence microscopy (Leica).

To detect the intracellular ROS after different treatments, 4T1 cells in 24-well plates were treated with different PCMs (ICG: 20 μg/mL) for 24 h and then incubated with ROS Assay Kit (DCFH-DA, 10 μM) for 1 h. After that, for the groups with laser treatment, the cells were irradiated with laser (808 nm, 1.5 W/cm^2, 5 min). Later, all the groups were immediately observed under fluorescence microscopy (Leica).

To quantify the cell apoptosis after different treatments, 4T1 cells in 24-well plates were treated with different PCMs (ICG: 20 μg/mL) for 24 h with or without laser irradiation (808 nm, 1.5 W/cm^2, 5 min). After that, the cells were collected and stained by Annexin V-FITC and PI according to the manufacturer's protocol, followed by detection with cytometry (Accuri C6).

To visualize the nuclear damage after different treatments, 4T1 cells in 96-well plates were treated with different PCMs (ICG: 20 μg/mL) for 24 h with or without laser irradiation (808 nm, 1.5 W/cm^2, 5 min). After that, the γ-H_2AX (H_2A histone family member X) in the cells were stained according to the manufacturer's protocol, followed by observation under fluorescence microscopy (Leica). The mean fluorescence intensity of cells was analyzed with Image J.

2.9. Animals and tumor xenograft model

Female Balb/c mice (4−5 weeks with a weight of 15–20 g) were supplied by the Beijing HFK Bioscience Co., Ltd. (Beijing, China). To establish the 4T1 subcutaneous tumor model, 1 × 10^6 murine breast cancer 4T1 cells were subcutaneously injected into the right lower limb of each mouse. Animals received care in accordance with the Guidance Suggestions for the Care and Use of Laboratory Animals.

2.10. In vivo biodistribution

To monitor the *in vivo* biodistribution of PCMs in the 4T1 subcutaneous tumor model, TPE-BICOOH@PCM and TPE-BICOOH@RPCMs NPs were injected intravenously through the tail vein into 4T1-tumor bearing mice (tumor diameter was 4–6 mm, 20 nmol TPE-BICOOH per mouse, n = 3). After 24 h, the mice were killed and the major organs as well as the tumors were collected and imaged with IVIS imaging system. The fluorescence intensity in tumor was quantified using the IVIS software.

2.11. In vivo tumor therapy in subcutaneous tumor models

When the 4T1 subcutaneous tumor volumes reached 90–100 mm^3, the tumor-bearing mice were randomly divided into seven groups (n = 5): (1) PBS + Laser, (2) I@PCM + Laser, (3) CI@PCM + Laser, (4) GI@PCM + Laser, (5) GCI@PCM + Laser, (6) GCI@RPCM and (7) GCI@RPCM + Laser. Each mouse was intravenously administered either PCMs (ICG, 2.6 mg/kg; GOx, 0.4 mg/kg; CPO, 8.6 U/kg; 100 μL) or PBS (100 μL) on day 0. At 24 h after administration of PCMs, group (1) to (5) were treated with laser irradiation (808 nm, 1.4 W/cm^2, 10 min) to make sure the maximum temperature was 45 ° C; group (7) with more tumor accumulation were treated with weaker laser irradiation (808 nm, 1.1 W/cm^2, 10 min) to make sure the maximum temperature was also 45 ° C. The lower power densities in animal studies here than those at cellular level was because that the ICG concentration was slightly higher than that at cellular level. During laser irradiation, the temperature of tumor surface was recorded with a thermal imager (A300, FLIR). Tumor volumes and body weight were measured every two days for 20 days, and the volume (mm^3) of the tumors was calculated as (tumor length) × (tumor width/2)^2. At day 23 and 24, the mice after different treatments were killed, and then the tumor tissues were weighed and stained with hematoxylin and eosin (H&E), terminal deoxynucleotidyl transferase dUTP nick end labeling (TUNEL) and Ki-67 immunohistochemistry to evaluate the anti-tumor effect. Furthermore, the tumor slices were stained by DCFH-DA to investigate the ROS level *in vivo*. The stained tumor slices were observed under optical microscopy.

2.12. Statistical analysis

Data were presented as mean ± standard deviation (SD). Statistical differences among groups were analyzed using a one-way analysis of variance (ANOVA) followed by a two-tailed Student's t-test.

3. Results

3.1. Characterization of GCI@RPCMs

GCI@RPCMs were prepared using the nanoprecipitation method. Specifically, a methanol solution containing PCMs, indocyanine green (ICG) and an aqueous solution of GOx and CPO were mixed and added into a 4 % ethanol solution of lipids. The mixture was then subjected to a rapid cooling process to obtain ~183 nm GCI@RPCMs with a negative surface charge (~-32 mV). Control samples, including GCI@PCMs (GOx/CPO/ICG/PCMs), GI@PCMs (GOx/ICG/PCMs), CI@PCMs (CPO/ICG/PCMs) and I@PCMs (ICG/PCMs) (Fig. 1a), were also prepared using the nanoprecipitation method. All the control samples exhibited narrow size distributions with hydrodynamic diameter of 150–180 nm. All the control samples (except I@PCM, slightly less negative, −28 mV) exhibited similar negative zeta potentials of −32 ~ −34 mV (Fig. 1b and c), similar to those of GCI@RPCMs, indicating comparable surface properties. NIR absorption curves with maximum absorption at 779 nm confirmed the successful encapsulation of ICG [30] (Fig. 1d). The entrapment efficiency (EE) and loading capacity (LC, w/w) of ICG, GOx and CPO in GCI@RPCMs (Fig. S1, Table S1) were determined to be 78.7 %/49.2 %, 21.5 %/6.72 %, and 21.5 %/(1.51 U/mg), respectively.

PCMs have been utilized to load chemotherapeutics like doxorubicin and ICG through hydrophobic interaction [25,26]. Considering the hydrophobic residues in the enzymes (GOx and CPO), we anticipate that GOx/CPO can also bind to PCMs through hydrophobic interaction. To investigate this, we performed molecular dynamics to examine the interactions between GOx/CPO and PCMs. After 100 ns of simulation, both GOx and CPO exhibited strong affinity to PCMs and the enzymes dispersed well in PCMs (Fig. 1e). Further calculation showed that the primary interactions of CPO and GOx against PCM were van der Waals energies (Fig. 1f). The van der Waals interactions regulate the hydrophobic effect [37], verifying our hypothesis that GOx/CPO can bind to PCMs through hydrophobic interaction. The total binding energies of PCMs to CPO were −166.4 kJ/mol and PCMs to GOx was −364.4 kJ/mol (Fig. 1g), indicating a strong interaction between enzymes and PCMs, where GOx had stronger binding interaction towards PCM NPs. The strong binding of GOx/CPO to PCM ensures their stable encapsulation within GCI@RPCMs. Furthermore, GCI@RPCMs demonstrated excellent stability, with only slight changes in hydrodynamic diameter and PDI values in water, PBS and 10 % FBS over 7 days (Fig. S1d).

Next, we evaluated the NIR-triggered enzyme release behavior of PCMs. Transmission electron microscope (TEM) revealed that the size of GCI@RPCMs was reduced by approximately 60 % after 10 min of NIR treatment, as the outer part of PCMs melted (Fig. 2a). The size reduction after NIR treatment was consistent with Liang's report [14]. Photothermal curves showed that GCI@RPCMs exhibited concentration-dependent and laser power-dependent photothermal behavior, with 20 μg mL^{-1} heating the solution to 53.1 ° C and 58.3 ° C under 808 nm NIR laser irradiation at 1 W cm^{-2} and 1.5 W cm^{-2}, respectively (Fig. 2b–S2a). In contrast, free ICG only heated the solutions to 45.0 ° C and 51.6 ° C under the same conditions (Figs. S2b and c). This indicates that the nano-formulation can enhance heat generation, likely due to higher fluorescence quenching and local ICG concentration in the nano-formulation (Fig. S2d) [38].

To track enzyme release from GCI@RPCMs after NIR treatment, GOx

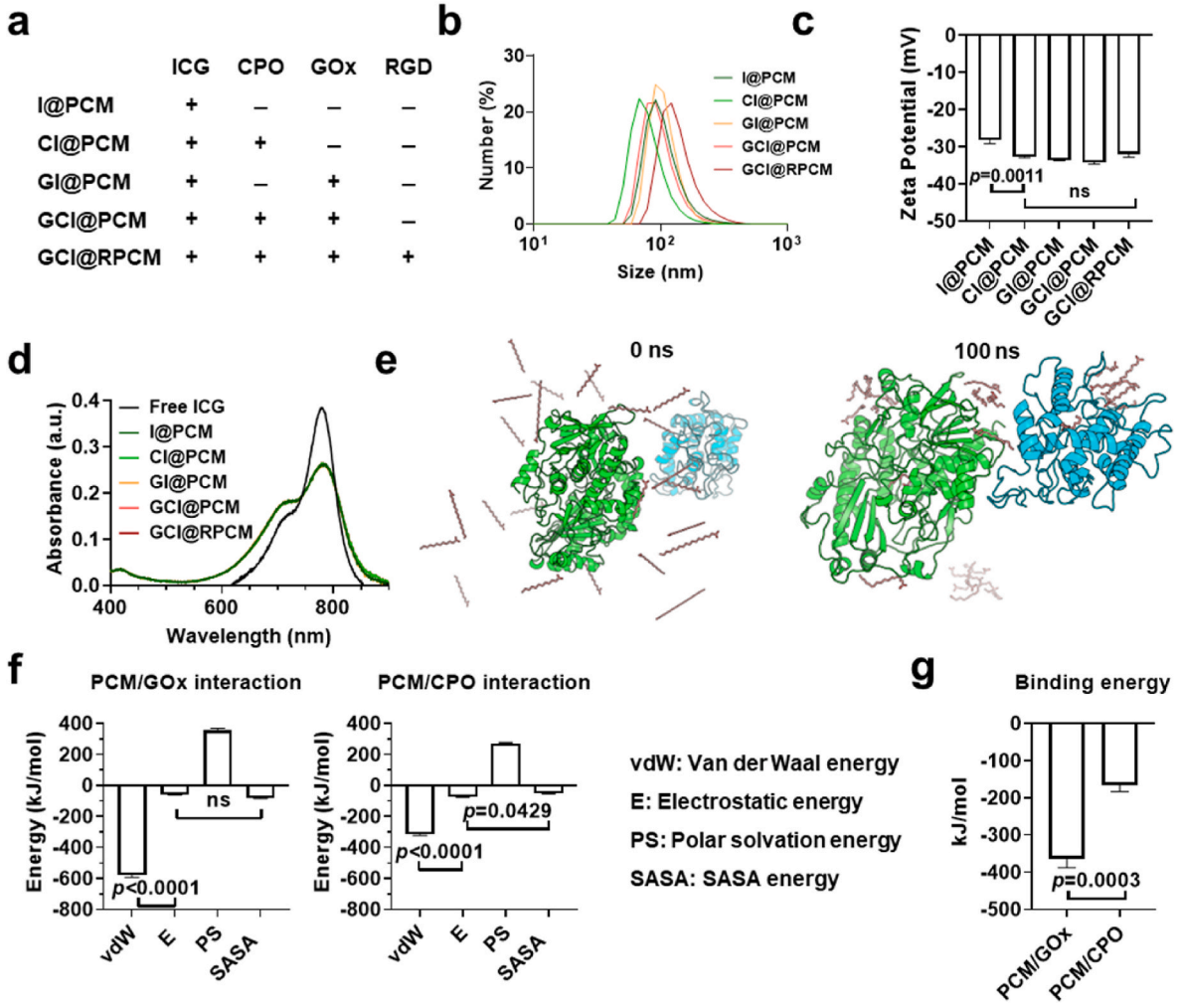

Fig. 1. Structural characterization of the GCI@RPCMs. (a) Schematic illustration of different PCMs. (b) Size distributions, (c) Zeta potentials and (d) NIR absorption spectra of the GCI@RPCMs and control samples. (e) The initial state (0 s) and equilibrium state (100 ns) of the solution simulation system. PCM is represented as sorrel sticks. CPO and GOx are represented with cyan and green proteins. (f) The calculated energies between PCM and CPO or GOx calculated by molecular dynamics. (g) The binding energies between PCM and CPO or GOx. Data was shown as mean ± SD. Statistical analysis was conducted by two-tail Student's t-test or one-way ANOVA analysis. (For interpretation of the references to color in this figure legend, the reader is referred to the Web version of this article.)

and CPO were labeled with FITC (FITC-GOx and FITC-CPO, Fig. 2c–S2e). Upon NIR irradiation, the FITC-GCI@RPCMs started to release their cargos at 2 min, and the release percentage reached 41 % at 10 min (Fig. 2c). In the absence of irradiation, the FITC-GCI@RPCMs remained super stable, releasing less than 1 % enzymes at 37 ° C after 10 min. The sharp "OFF-ON" drug-release pattern of PCMs demonstrates the high stability and NIR-response of PCMs.

Further, we investigated the NIR-responsive enzyme activity of GCI@RPCMs. The enzyme activity of GOx/CPO cascade is usually detected through the decolorization of acid orange 7 (AO7) by generated HClO [34], but the ICG in the NIR-responsive PCMs can interfere with the absorption of AO7, which makes it difficult to quantify the enzyme activity. Hence, we chose to study thermo-responsive enzyme activity instead. To achieve this, we synthesized GC@PCMs (~150 nm, −26 mV) (Fig. 2e) to replace GCI@RPCMs and used free GOx and CPO as the control to evaluate the enzyme activity. As the melting point of PCMs is around 43 ° C, we chose to investigate the enzyme activity at temperatures below and above 43 ° C (25 ° C, 37 ° C and 45 ° C). As shown in Fig. 2f,g and S3a-c, the decolorization efficiency of GC@PCM was barely detectable at 25 or 37 ° C, while that of free GOx/CPO increases with temperature, indicating that the enzymes were stably encapsulated in GC@PCM at these two temperatures. At 45 ° C, the enzymes in the GC@PCMs can be released and the decoloring efficiency of PCMs was very similar to that of free GOx/CPO (~30 %), demonstrating that the excellent thermo-responsive enzyme activity of GC@PCMs (Fig. 2h and i). The similar enzyme activity of GC@PCMs and free GOx/CPO at 45 ° C and similar Michaelis-Menten constant (K_m) values of free GOx/CPO (3.46 mg/mL) and GC@PCMs (4.86 mg/mL) (Fig. S3d) indicated that the nanoparticle synthesis courses do not affect the enzyme activity. As GCI@RPCMs and GC@PCMs have similar synthetic protocol, we inferred that the GCI@RPCMs displayed similar enzyme activity as the free GOx/CPO. It is worth noting that GOx and CPO can bear 45 ° C treatment in thermo-response, as the optimal catalytic temperature of GOx is 45 ° C [39] and CPO can retain 90 % activity at 40 ° C after 12 h of incubation [40]. In addition, the negligible decolaration of AO7 by single GOx or CPO treatment emphasized that both GOx and CPO were essential for the activity of the enzyme cascades(Fig. S3e). Further, we also investigated the effect of pH on enzyme release and activity. It was found that negligible protein was released from FITC-GCI@PCM NPs at pH = 3 or 5 (Fig. S4a). The enzyme activity reduced to 72.4 % and 80.9 % at pH = 3 and pH = 5, respectively (Figs. S4b–e), indicating the acidic pH can slightly reduce the enzyme activity of GOx/CPO enzyme cascade. These results demonstrated that GCI@RPCMs are super-stable and NIR-responsive enzyme delivery systems.

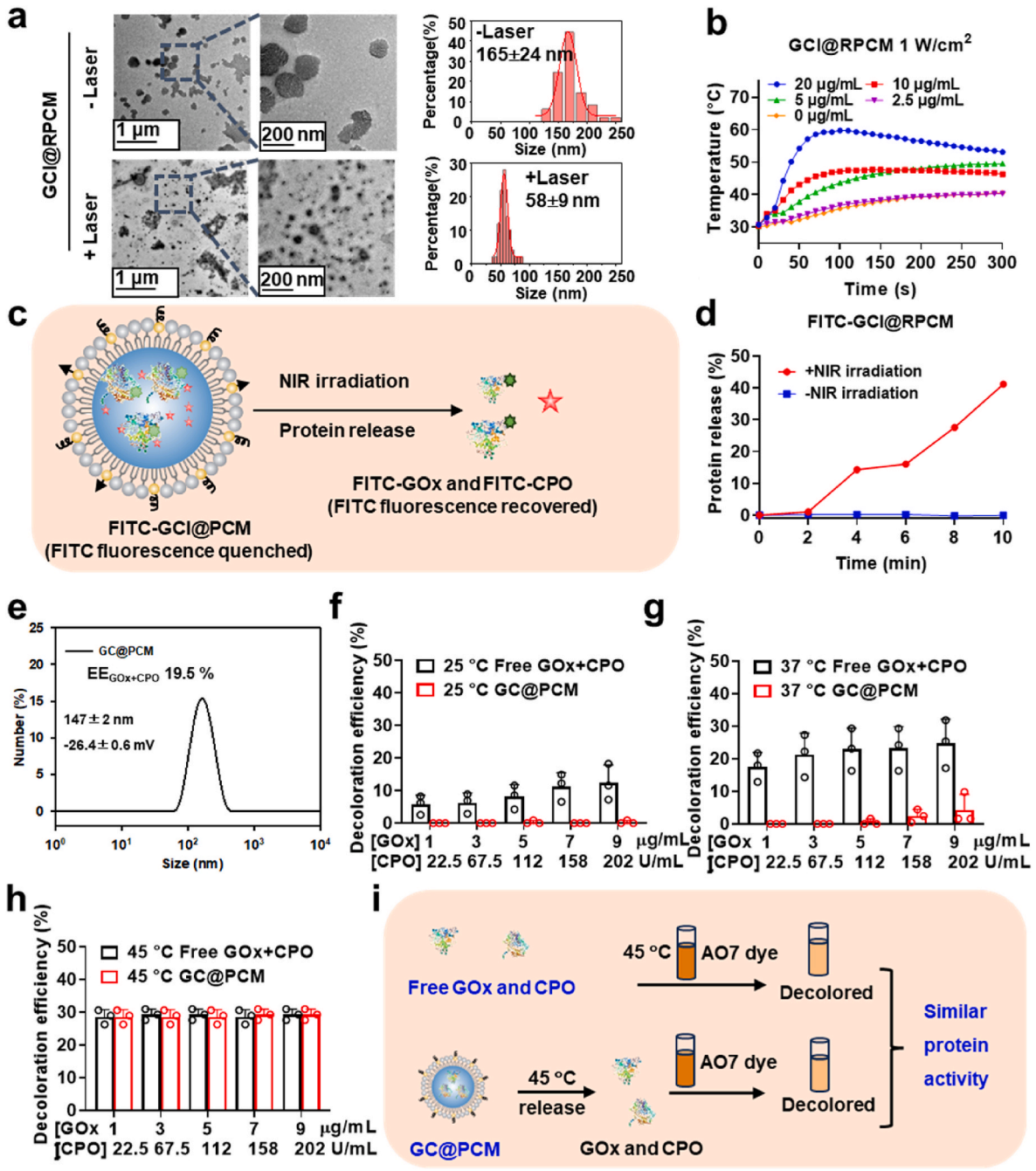

Fig. 2. NIR-responsive characterizations of the GCI@RPCMs. (a) TEM images of GCI@RPCMs without and with irradiation (808 nm, 1.4 W/cm^2, 10 min), particle size distribution histograms and Gaussian fitting curves. (b) Concentration-dependent photothermal behavior of GCI@RPCMs upon irradiation (808 nm, 1 W/cm^2, 10 min). (c) Schematic illustration of NIR-responsive enzyme release. (d) Enzyme release kinetics from FTIC-GCI@RPCMs after NIR irradiation (808 nm, 0.8 W/cm^2, 10 min). (e) Representative size distribution of GC@PCMs. (f) The decolorization efficiency of AO7 treated by free GOx and CPO mixture or GC@PCMs at 25 °C, (g) 37 °C and (h) 45 °C. Data was shown as mean ± SD. (i) Schematic illustration of thermo-responsive enzyme release and activity measurement.

3.2. NIR light-activated enzymatic dynamic therapy in vitro

Effective cellular uptake of nanomedicines is the perquisite for their therapeutic effect. To investigate the cellular uptake of arginylglycylaspartic acid (RGD) ligand-modified PCMs (GCI@RPCMs), we used fluorescent TPE-BICOOH@RPCMs (Fig. S5) instead, which contained fluorophore TPE-BICOOH [36] and exhibited strong fluorescence emission due to aggregation-induced emission effect [41–43] of TPE-BICOOH. Meanwhile, PCMs without RGD ligand modification were also labeled with TPE-BICOOH to obtain TPE-BICOOH@PCMs. Both types of PCMs were then incubated with 4T1 cells for 2–12 h, exhibiting time-dependent cellular uptake. The TPE-BICOOH@RPCM group exhibited stronger green fluorescence, indicating higher uptake (Fig. 3a and b), which was attributed to the RGD ligand on the RPCMs binding to the $\alpha_v\beta_3$ integrin overexpressed in the 4T1 cell membrane. Then RGD blocking assay [17] further demonstrated that the higher uptake in the TPE-BICOOH@RPCM group was mediated by RGD ligands (Fig. S6). Moreover, both TPE-BICOOH@RPCMs and TPE-BICOOH@PCMs showed low uptake in MCF-10A cells (Fig. 3c–S7). Further quantification results demonstrated that the TPE-BICOOH@RPCMs exhibited 2.8-fold more uptake in 4T1 cells than in MCF-10A cells, indicating the great tumor cell selectivity of RGD ligand-modified PCMs in 4T1 cells.

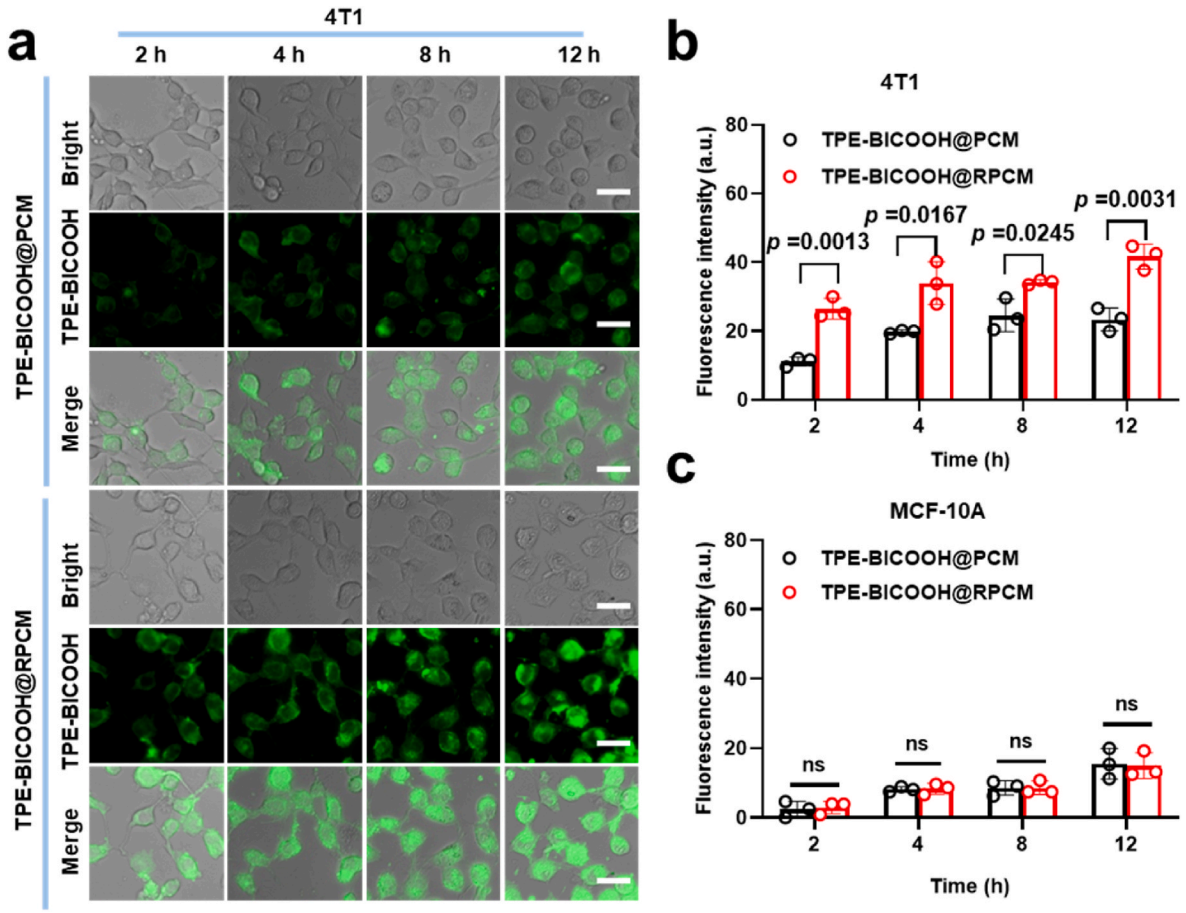

Fig. 3. Cellular uptake studies of RPCMs. (a) Time-dependent cellular uptake of TPE-BICOOH@RPCMs and TPE-BICOOH@PCMs after incubation with 4T1 cells. Scale bar: 20 μm. (b) Quantification of the mean fluorescence intensity of the 4T1 cells after different treatments. (c) Quantification of the mean fluorescence intensity of the MCF-10A cells after different treatments. Data was shown as mean ± SD. Statistical analysis was conducted by two-tail Student's t-test or one-way ANOVA analysis.

Given the selective uptake of RGD ligand-modified PCMs in the 4T1 cells, we further investigated their tumor cell inhibition through methyl thiazolyl tetrazolium (MTT) assay, live/die cell staining and Annexin V-fluorescein isothiocyanate (Annexin V-FITC)/propidium iodide (PI) fluorescence staining. Meanwhile, 4T1 cells treated with GCI@PCMs, GI@PCMs, CI@PCMs and I@PCMs were set as control groups to investigate the role of the components in GCI@RPCMs. To eliminate the photothermal therapeutic effect [44] and enable active enzyme release from PCMs, we chose to irradiate PCMs-treated 4T1 cells with a maximum temperature of 45 °C. MTT assay showed that the GCI@RPCMs demonstrated laser and concentration dependent cytotoxicity against 4T1 cells. Without laser irradiation, the cell viability of all the groups were nearly 100 %, indicating that the PCMs were very stable and negligible enzymes were released at 37 ° C (Fig. 4a). Upon irradiation, GCI@RPCMs lead to ~50 % cell death when ICG was 20 μg mL^{-1}, while GCI@PCMs only lead to ~20 % cell death (Fig. 4b), attributing to RGD ligand-mediated enhanced uptake of enzymes. Negligible cytotoxicity of GI@PCM and CI@PCM-treated groups after NIR laser irradiation demonstrated the necessity of cascade enzymes (GOx and CPO) for effective treatment. Negligible cytotoxicity of I@PCM-treated group in the presence of laser irradiation demonstrated that ICG did not exhibit photothermal or photodynamic therapeutic effect against 4T1 cells in our conditions. Further, live/die cell staining of different groups verified the strong tumor cell inhibition by GCI@RPCMs after NIR laser irradiation (Fig. 4c–S8a). Moreover, the flow cytometry assay with Annexin V-fluorescein isothiocyanate (Annexin V-FITC)/propidium iodide (PI) fluorescence staining demonstrated that 4T1 cells treated with GCI@RPCM exhibited the highest cell apoptosis and necrosis ratio upon laser irradiation (Fig. 5d, S8b). These results demonstrated that the tumor cell inhibition of GCI@RPCM exhibits NIR-responsive enzyme cascade therapy, which was due to its tumor-cell selective uptake and released enzyme cascade upon NIR laser irradiation.

Moreover, we studied the antitumor mechanism of GCI@RPCM. We first monitored the content of intracellular reactive oxygen species (ROS) after different treatments by ROS probe 2′,7′-dichlorofluorescin diacetate (DCFH-DA). As shown in Fig. 5a, GCI@RPCM and GCI@PCM groups after laser irradiation (808 nm, 1.5 W cm^{-2}, 5 min) had strong ROS signals arise probably from HClO, while GI@PCM had weak ROS signals probably from H_2O_2 [32]. The negligible ROS signals from I@PCM group indicated that the ROS from ICG in GCI@RPCMs is little and the ROS signals of GCI@RPCMs were primarily from the enzyme cascades. Meanwhile, the ROS of all the groups without laser irradiation was negligible. Afterward, we evaluated the intracellular DNA damage by ROS through staining γ-H2AX (H2A histone family member X), a marker of DNA double-stranded breaks. Upon irradiation, the GCI@RPCM group also exhibited the strongest fluorescence, indicating the obvious DNA damage of GCI@RPCM group (Fig. 5b and c). In the absence of laser irradiation, no DNA damage was detected (Fig. S9). These results demonstrated that GCI@RPCMs generate ROS with NIR response, which lead to NIR-responsive intracellular DNA damage and tumor cell death.

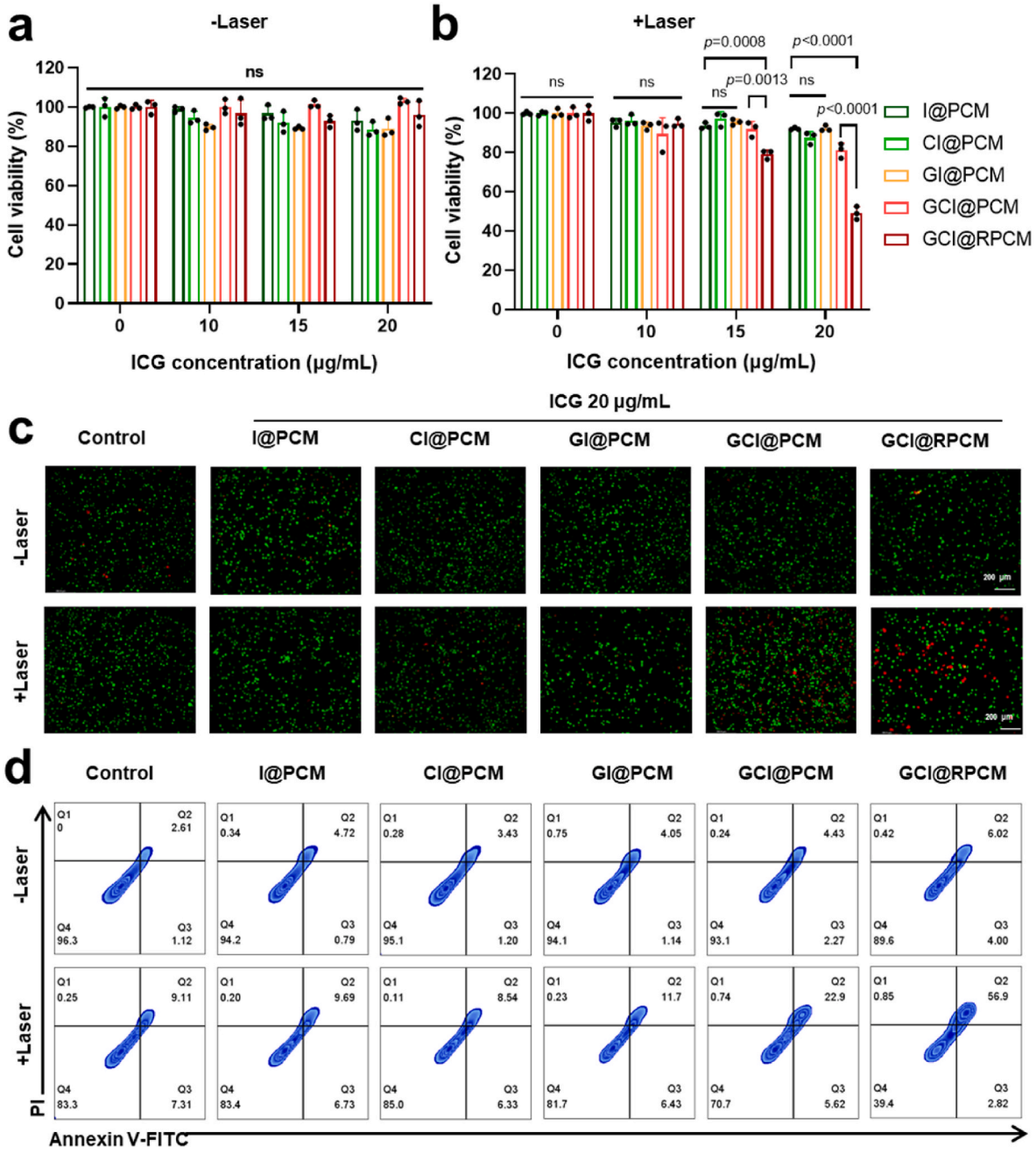

Fig. 4. *In vitro* tumor cell inhibition by NIR-responsive GCI@RPCMs. (a) The cell viability of 4T1 cells after treatment with different PCMs without or (b) with laser irradiation (808 nm, 1.5 W/cm^2, 5 min). (c) The live/die cell staining of 4T1 cells after treatment with different PCMs (ICG: 20 μg/mL) without or with laser irradiation (808 nm, 1.5 W/cm^2, 5 min). Data was shown as mean ± SD. Statistical analysis was conducted by two-tail Student's t-test or one-way ANOVA analysis. (d) The Annexin V-FITC/PI staining of 4T1 cells after treatment with different PCMs (ICG: 20 μg/mL) without or with laser irradiation (808 nm, 1.5 W cm^{-2}, 5 min).

3.3. NIR-responsive enzymatic dynamic therapy in vivo

To evaluate the *in vivo* biodistribution and tumor accumulation of PCMs, fluorescent TPE-BICOOH@RPCMs and TPE-BICOOH@PCMs were injected into 4T1-tumor-bearing mice upon intravenous administration. At 24 h after injection, the mice were killed and the *ex vivo* imaging showed that both NPs distributed in liver, kidneys and tumor, and the tumor accumulation of TPE@RPCM group was 1.8 times that of TPE@PCM group (Fig. S10), indicating the RGD ligand can increase the tumor accumulation of PCM NPs.

To evaluate the therapeutic efficiency of GCI@RPCMs with NIR laser irradiation against 4T1-tumor-bearing mice, we set the following groups as control: PBS with irradiation (group 1), I@PCM with irradiation (group 2), CI@PCM with irradiation (group 3), GI@PCM with irradiation (group 4), GCI@PCM with irradiation (group 5) and GCI@RPCM without irradiation (group 6) (Fig. 6a). To eliminate the difference of photothermal effect in groups treated with different NPs, the laser power density was mildly tuned so that the maximum temperatures on the groups 2 to 5 and 7 were all at around 45 °C (Fig. 6b and c). In contrast, the PBS treatment (group 1) showed negligible temperature increase (<2 °C). Tumor growth curves after different treatments were monitored for 20 days. During the 20-day monitoring, all the mice survived, and the tumor volumes were all less than 2000 mm^3 (Fig. S11). The GCI@RPCM group without irradiation (group 6) was not significantly different from PBS group (group 1), indicating the high stability of GCI@RPCMs *in vivo* (Fig. 6d–S12a). With irradiation, negligible tumor inhibition was

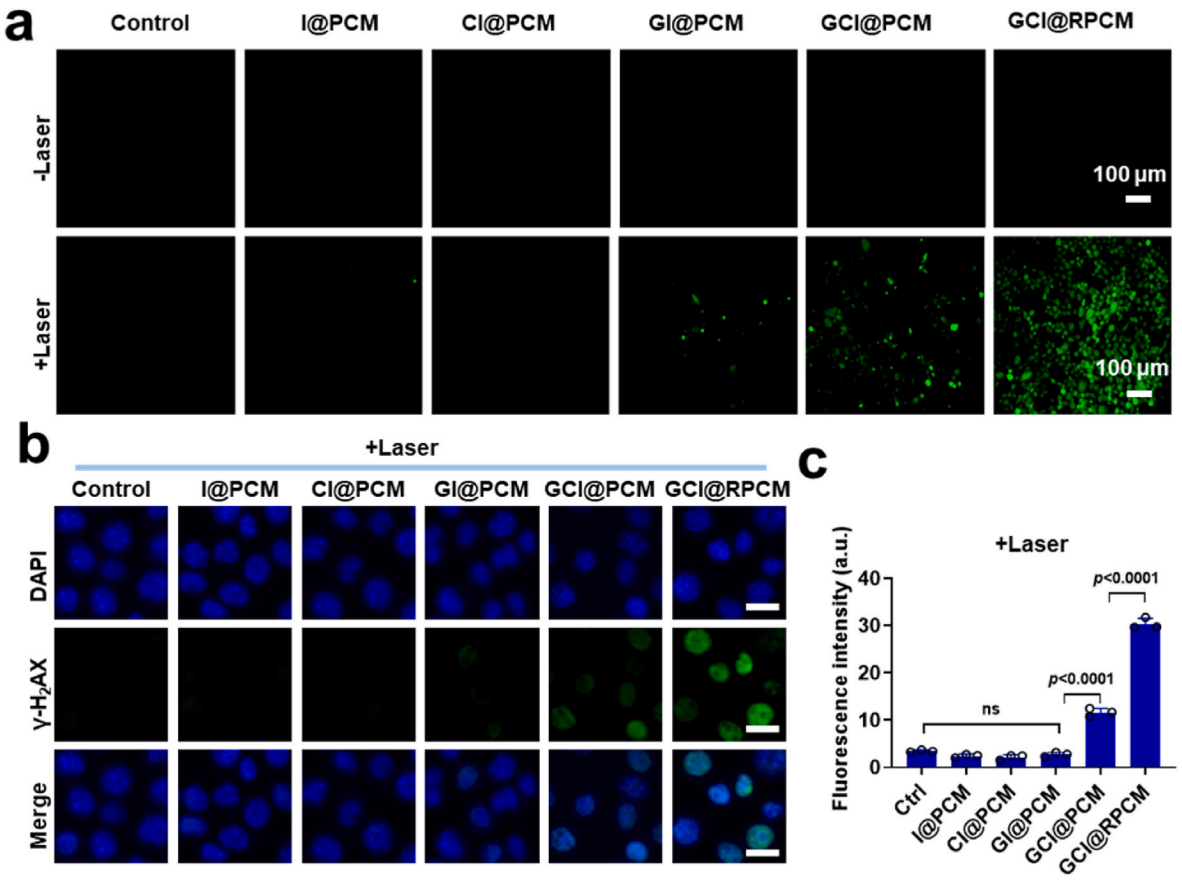

Fig. 5. The anti-tumor mechanism of NIR-responsive GCI@RPCMs. (a) Intracellular ROS detection (by DCFH-DA) of 4T1 cells after different treatments (ICG: 20 μg/mL). Laser irradiation: 808 nm, 1.5 W cm^{-2}, 5 min. (b) The nuclear damage assay (by γ-H2AX staining) of 4T1 cells after different treatments with laser irradiation (808 nm, 1.5 W cm^{-2}, 5 min). Scale bar, 20 μm. (c) Quantified nuclear damage of 4T1 cells in (b). Data was shown as mean ± SD. Statistical analysis was conducted by two-tail Student's t-test or one-way ANOVA analysis.

observed in I@PCM (group 2), which indicates photothermal effect of I@PCM alone is not enough to induce tumor inhibition. CI@PCM with irradiation (group 3) also showed negligible tumor inhibition, which was probably due to inefficient generation of HClO in the absence of GOx. Slight tumor inhibition (35.2 %) was observed in GI@PCM with irradiation (group 4), owing to the generated H_2O_2 in the presence of glucose in the tumor tissue. GCI@PCM with irradiation (group 5) showed much stronger tumor inhibition (51.5 %) due to the cascade of GOx/CPO, with more generation of HClO in the tumor tissue. GCI@RPCM with irradiation (group 7) showed strongest tumor inhibition (100 %) due to the enhanced delivery of GOx/CPO cascade, leading to highest generation of HClO. Moreover, the tumors after various treatments were harvested at the end of the treatment, and the weights of the tumors after different treatments validated the excellent therapeutic effect of GCI@RPCMs (Fig. 6e and f), which was similar to the results of tumor volumes.

To further demonstrate the therapeutic effects, the excised tumors (except group 7, whose tumors were completely eradicated) were analyzed by hematoxylin and eosin (H&E) staining, ROS, Ki-67 and terminal-deoxynucleotidyl transferase-mediated nick end labeling (TUNEL) immunofluorescent staining. H&E staining showed that significant nuclear dissociation was observed in the GCI@PCM group with irradiation (group 5) (Fig. 6g). ROS staining showed that GCI@PCM group showed abundant ROS distribution both in nucleus and cytoplasm, where GI@PCM group also showed some ROS, and the other groups showed negligible ROS. For Ki-67 staining, GCI@PCM group showed negligible Ki-67 expression, while the other groups all showed strong Ki-67 expression. TUNEL staining indicated the apoptosis of tumor cells in GCI@PCM (group 5), but not in group 1–4. Taken together, the killing effect of tumors by GCI@RPCM NPs upon laser irradiation is due to the effective accumulation and release of GOx/CPO in the tumor tissue and the generated ROS, and independent of photothermal effect. The strong ROS led to downregulation of Ki-67 and substantial apoptosis of tumor cells.

In addition, no noticeable weight loss in mice(Fig. S12c), no histological abnormality observed in major organs (Fig. S13) and low hemolysis (<5 %) after various treatments and negligible hemolysis (Fig. S14) indicated the good biocompatibility of GCI@RPCMs.

4. Conclusions

In summary, we developed highly stable and NIR-responsive phase transition materials for delivering enzyme cascade toward tumor therapy. The RGD ligand surface modification of materials increased the *in vitro* cellular uptake of NPs and *in vivo* tumor targeting. The enzyme cascades (GOx and CPO) were stably encapsulated in the RPCMs mainly through van der Waals interaction. Upon NIR laser irradiation, the photothermal agent (ICG) in the phase transition materials (GCI@RPCMs) heated the PCMs and released active enzymes for tumor therapy. In vivo studies demonstrated that the GCI@RPCMs exhibited excellent biocompatibility and strong NIR-responsive tumor inhibition.

Compared to traditional ROS(H_2O_2) carrier, the nanoplatform in this work has three unique advantages and improvements: (1) GOx/CPO cascade instead of GOx alone is used in the nanomedicine, where GOx generates H_2O_2 in the tumor tissue, but GOx/CPO generates HClO in the tumor tissue; (2) the tumor killing effect of HClO is stronger than H_2O_2; (3) the ROS generation is strictly controlled by laser irradiation, which endows the nanomedicine with great safety and tumor selectivity.

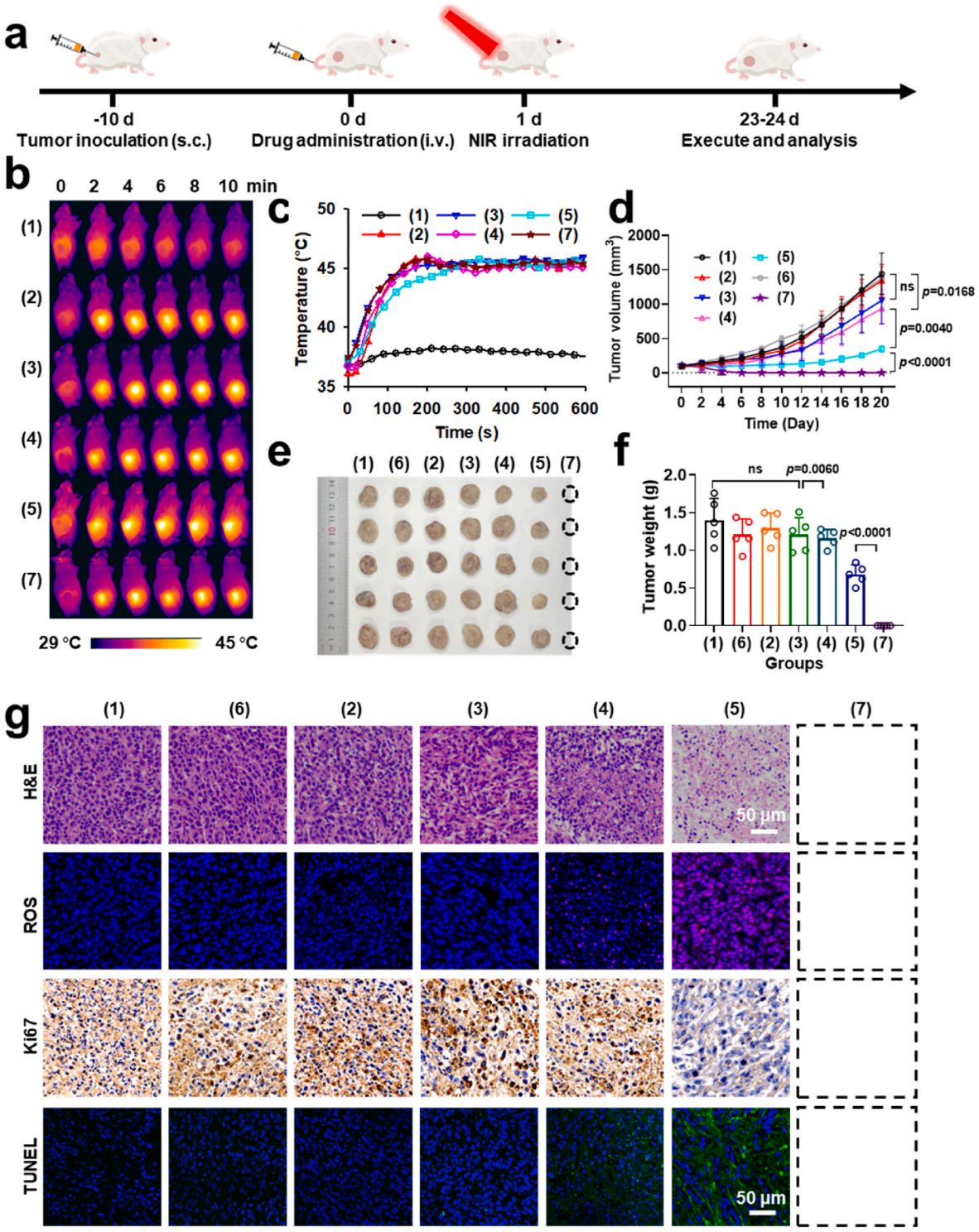

Fig. 6. NIR-responsive enzymatic dynamic therapy *in vivo*. (a) Schematic description of the establishment of 4T1 tumor xenograft and the treatment procedures. (b) Infrared thermal images and (c) temperature profiles after different treatments, followed by exposure to 808 nm laser irradiation (1.4 W/cm^2, 10 min for groups 1–5; 1.1 W/cm^2, 10 min for group 7). (d) Tumor growth profiles of 4T1-tumor-bearing mice after various treatments. (e) Tumor images and (f) the average tumor weights excised on day 23 and 24 from the mice receiving various treatments. (g) H&E staining, ROS, Ki-67 and TUNEL immunofluorescent staining of tumor slices. The numbers (1–7) represented different groups: 1. PBS + Laser; 2. I@PCM + Laser; 3. CI@PCM + Laser; 4. GI@PCM + Laser; 5. GCI@PCM + Laser; 6. GCI@RPCM; 7. GCI@RPCM + Laser. Data was shown as mean ± SD. Statistical analysis was conducted by two-tail Student's t-test or one-way ANOVA analysis.

We believe that the NIR-responsive PCMs can be developed as a universal platform to deliver active therapeutic enzymes for the treatment of various diseases. Given the limited penetration of NIR, ultrasound [45] and X-ray [46–48] with unlimited penetration depth can further endow responsive PCMs with high clinical translation potential.

CRediT authorship contribution statement

Yuqiong Xia: Writing – review & editing, Writing – original draft, Supervision, Funding acquisition, Conceptualization. **Chang Liu:** Visualization, Investigation. **Xuejuan Zhao:** Conceptualization. **Keyun Wu:**

Validation. **Jianxia Cao:** Investigation. **Yutian Cao:** Investigation. **Cheng Zhu:** Writing – review & editing, Software. **Xianghan Zhang:** Writing – review & editing, Supervision, Funding acquisition.

Funding

This work is supported by Key Research and Development Program of Shaanxi (2024SF2-GJHX-30), Shaanxi Fundamental Science Research Project for Chemistry & Biology (Grant No. 22JHQ076), GuangDong Basic and Applied Basic Research Foundation (2023A1515030207), National Natural Science Foundation of China (32371433, 22077094), the Fundamental Research Funds for the Central Universities (No. ZYTS24153). Xidian University Specially Funded Project for Interdisciplinary Exploration (TZJH2024031, TZJH2024035). The molecular dynamics in this work was carried out at National Supercomputer Center and the calculations were performed on TianHe-1(A).

Declaration of competing interest

The authors have no competing interests.

Appendix B. Supplementary data

Supplementary data to this article can be found online at https://doi.org/10.1016/j.mtbio.2024.101345.

Data availability

Data will be made available on request.

References

[1] H. Sung, J. Ferlay, R.L. Siegel, M. Laversanne, I. Soerjomataram, A. Jemal, F. Bray, Global cancer statistics 2020: GLOBOCAN estimates of incidence and mortality worldwide for 36 cancers in 185 countries, CA A Cancer J. Clin. 71 (3) (2021) 209–249.
[2] B. Liu, S. Liang, Z. Wang, Q. Sun, F. He, S. Gai, P. Yang, Z. Cheng, J. Lin, A tumor-microenvironment-responsive nanocomposite for hydrogen sulfide gas and trimodal-enhanced enzyme dynamic therapy, Adv. Mater. 33 (30) (2021) e2101223.
[3] B. Liu, Y. Bian, M. Yuan, Y. Zhu, S. Liu, H. Ding, S. Gai, P. Yang, Z. Cheng, J. Lin, L-buthionine sulfoximine encapsulated hollow calcium peroxide as a chloroperoxidase nanocarrier for enhanced enzyme dynamic therapy, Biomaterials 289 (2022) 121746.
[4] T. Peng, Y. Huang, X. Feng, C. Zhu, S. Yin, X. Wang, X. Bai, X. Pan, C. Wu, TPGS/hyaluronic acid dual-functionalized PLGA nanoparticles delivered through dissolving microneedles for markedly improved chemo-photothermal combined therapy of superficial tumor, Acta Pharm. Sin. B 11 (10) (2021) 3297–3309.
[5] J. Peng, J. Zhou, X. Liu, X. Zhang, X. Zhou, Z. Gong, Y. Chen, X. Shen, Y. Chen, A biomimetic nanocarrier facilitates glucose consumption and reactive oxide species accumulation in enzyme therapy for colorectal cancer, J. Contr. Release 367 (2024) 76–92.
[6] J. Zhang, L. Sun, L. Jiang, X. Xie, Y. Wang, R. Wu, Q. Tang, S. Sun, S. Zhu, X. Liang, L. Cui, Regulation of CTLs/tregs via highly stable and ultrasound-responsive cerasomal nano-modulators for enhanced colorectal cancer immunotherapy, Adv. Sci. 11 (22) (2024) 2400485.
[7] Y. Xia, Y. Wu, J. Cao, J. Wang, Z. Chen, C. Li, X. Zhang, Liposomal glucose oxidase for enhanced photothermal therapy and photodynamic therapy against breast tumors, ACS Biomater. Sci. Eng. 8 (5) (2022) 1892–1906.
[8] Y. Xia, K. Wu, C. Liu, X. Zhao, J. Wang, J. Cao, Z. Chen, M. Fang, J. Yu, C. Zhu, X. Zhang, Z. Wang, Filamentous-actin-mimicking nanoplatform for enhanced cytosolic protein delivery, Adv. Sci. 11 (10) (2024) 2305600.
[9] C. Zhao, C. Wang, W. Shan, W. Wang, H. Deng, Fusogenic lipid nanovesicle for biomacromolecular delivery, Nano Lett. 24 (28) (2024) 8609–8618.
[10] C. Wang, C. Zhao, W. Wang, X. Liu, H. Deng, Biomimetic noncationic lipid nanoparticles for mRNA delivery, Proc. Natl. Acad. Sci. U.S.A. 120 (51) (2023) e2311276120.
[11] P. Gong, H. Cui, C. Li, S. Song, Y. Gong, J. Li, B. Wang, F. Liu, D. Wang, Z. Liu, Self-stablized monodispersing nano-MOFs for controlled enzyme delivery, Chem. Eng. J. 489 (2024) 150941.
[12] K. Ma, X. Zhang, J. Ji, L. Han, X. Ding, W. Xie, Application and research progress of phase change materials in biomedical field, Biomater. Sci. 9 (17) (2021) 5762–5780.
[13] C. Cao, N. Yang, H. Dai, H. Huang, X. Song, Q. Zhang, X. Dong, Recent advances in phase change material based nanoplatforms for cancer therapy, Nanoscale Adv. 3 (1) (2021) 106–122.
[14] G. Qing, X. Zhao, N. Gong, J. Chen, X. Li, Y. Gan, Y. Wang, Z. Zhang, Y. Zhang, W. Guo, Y. Luo, X.J. Liang, Thermo-responsive triple-function nanotransporter for efficient chemo-photothermal therapy of multidrug-resistant bacterial infection, Nat. Commun. 10 (1) (2019) 4336.
[15] H.S. Jung, P. Verwilst, A. Sharma, J. Shin, J.L. Sessler, J.S. Kim, Organic molecule-based photothermal agents: an expanding photothermal therapy universe, Chem. Soc. Rev. 47 (7) (2018) 2280–2297.
[16] Z. Shi, M. Luo, Q. Huang, C. Ding, W. Wang, Y. Wu, J. Luo, C. Lin, T. Chen, X. Zeng, L. Mei, Y. Zhao, H. Chen, NIR-dye bridged human serum albumin reassemblies for effective photothermal therapy of tumor, Nat. Commun. 14 (1) (2023) 6567.
[17] X. Zhang, S. Zhao, Z. Gao, J. Zhou, Y. Xia, J. Tian, C. Shi, Z. Wang, Liposome trade-off strategy in mitochondria-targeted NIR-cyanine: balancing blood circulation and cell retention for enhanced antitumor phototherapy in vivo, Nano Res. 14 (7) (2021) 2432–2440.
[18] N. Yang, H. Li, C. Cao, L. Zhao, X. Song, W. Wang, W. Xu, Y. Zhang, P. Chen, X. Dong, Tumor microenvironment-activated theranostic nanoreactor for NIR-II Photoacoustic imaging-guided tumor-specific photothermal therapy, Fundam. Res. 4 (1) (2024) 178–187.
[19] X. An, Z. Chen, Y. Luo, P. Yang, Z. Yang, T. Ji, Y. Chi, S. Wang, R. Zhang, Z. Wang, J. Li, Light-Activated in situ vaccine with enhanced cytotoxic T lymphocyte infiltration and function for potent cancer immunotherapy, Adv. Sci. 11 (2024) 2403158.
[20] P. Yang, F. Du, W. Zhang, W. Liu, Z. Ye, H. Fan, J. Yu, K.M.v. Deneen, Z. Wang, P. Ning, Ingenious designed a HER2-Specific macrophage biomimetic multifunctional nanoplatform for enhanced bio-photothermal synergistic therapy in HER2 positive breast cancer, Materials Today Bio 26 (2024) 101095.
[21] Z. Zhang, Y. Du, X. Shi, K. Wang, Q. Qu, Q. Liang, X. Ma, K. He, C. Chi, J. Tang, B. Liu, J. Ji, J. Wang, J. Dong, Z. Hu, J. Tian, NIR-II light in clinical oncology: opportunities and challenges, Nat. Rev. Clin. Oncol. 21 (6) (2024) 449–467.
[22] A. Raza, U. Hayat, T. Rasheed, M. Bilal, H.M.N. Iqbal, "Smart" materials-based near-infrared light-responsive drug delivery systems for cancer treatment: a review, J. Mater. Res. Technol. 8 (1) (2019) 1497–1509.
[23] W. Zhao, Y. Zhao, Q. Wang, T. Liu, J. Sun, R. Zhang, Remote light-responsive nanocarriers for controlled drug delivery: advances and perspectives, Small 15 (45) (2019) e1903060.
[24] J. Son, G. Yi, J. Yoo, C. Park, H. Koo, H.S. Choi, Light-responsive nanomedicine for biophotonic imaging and targeted therapy, Adv. Drug Deliv. Rev. 138 (2019) 133–147.
[25] Y. Dai, J. Su, K. Wu, W. Ma, B. Wang, M. Li, P. Sun, Q. Shen, Q. Wang, Q. Fan, Multifunctional thermosensitive liposomes based on natural phase-change material: near-infrared light-triggered drug release and multimodal imaging-guided cancer combination therapy, ACS Appl. Mater. Interfaces 11 (11) (2019) 10540–10553.
[26] C. Zhu, D. Huo, Q. Chen, J. Xue, S. Shen, Y. Xia, A eutectic mixture of natural fatty acids can serve as the gating material for near-infrared-triggered drug release, Adv. Mater. 29 (40) (2017) 1703702.
[27] B. Shi, N. Ren, L. Gu, G. Xu, R. Wang, T. Zhu, Y. Zhu, C. Fan, C. Zhao, H. Tian, Theranostic nanoplatform with hydrogen sulfide activatable NIR responsiveness for imaging-guided on-demand drug release, Angew. Chem., Int. Ed. Engl. 58 (47) (2019) 16826–16830.
[28] S. Zhang, C. Cao, X. Lv, H. Dai, Z. Zhong, C. Liang, W. Wang, W. Huang, X. Song, X. Dong, A H2O2 self-sufficient nanoplatform with domino effects for thermal-responsive enhanced chemodynamic therapy, Chem. Sci. 11 (7) (2020) 1926–1934.
[29] X. Ji, Y. Ma, W. Liu, L. Liu, H. Yang, J. Wu, X. Zong, J. Dai, W. Xue, In situ cell membrane fusion for engineered tumor cells by worm-like nanocell mimics, ACS Nano 14 (6) (2020) 7462–7474.
[30] M. Zheng, C. Yue, Y. Ma, P. Gong, P. Zhao, C. Zheng, Z. Sheng, P. Zhang, Z. Wang, L. Cai, Single-step assembly of DOX/ICG loaded lipid–polymer nanoparticles for highly effective chemo-photothermal combination therapy, ACS Nano 7 (3) (2013) 2056–2067.
[31] M. Wu, Q. Wang, S. Chen, Z. Zhou, J. Li, H. Sun, J. Liu, G. Wang, F. Zhou, M. Sun, Metabolic intervention liposome for targeting glutamine-addiction of breast cancer, J. Contr. Release 350 (2022) 1–10.
[32] L.H. Fu, C. Qi, Y.R. Hu, J. Lin, P. Huang, Glucose oxidase-instructed multimodal synergistic cancer therapy, Adv. Mater. 31 (21) (2019) 1808325.
[33] Q. Zhang, J. Wu, J. Wang, X. Wang, C. Wu, M. Chen, Q. Wu, M.S. Lesniak, Y. Mi, Y. Cheng, Q. Wang, A neutrophil-inspired supramolecular nanogel for magnetocaloric-enzymatic tandem therapy, Angew. Chem., Int. Ed. Engl. 59 (9) (2020) 3732–3738.
[34] C. Zhang, L. Zhang, W. Wu, F. Gao, R.Q. Li, W. Song, Z.N. Zhuang, C.J. Liu, X. Z. Zhang, Artificial super neutrophils for inflammation targeting and HClO generation against tumors and infections, Adv. Mater. 31 (19) (2019) e1901179.
[35] G.T. Hermanson, Bioconjugate Techniques, third ed., Elsevier Inc., London, 2013.
[36] X. Zhang, B. Wang, Y. Xia, S. Zhao, Z. Tian, P. Ning, Z. Wang, In vivo and in situ activated aggregation-induced emission probes for sensitive tumor imaging using tetraphenylethene-functionalized trimethincyanines-encapsulated liposomes, ACS Appl. Mater. Interfaces 10 (30) (2018) 25146–25153.
[37] C.J. van Oss, D.R. Absolom, A.W. Neumann, The "hydrophobic effect": Essentially a van der Waals interaction, Colloid Polym. Sci. 258 (4) (1980) 424–427.
[38] H. Zhao, J. Xu, Y. Wang, C. Sun, L. Bao, Y. Zhao, X. Yang, Y. Zhao, A photosensitizer discretely loaded nanoaggregate with robust photodynamic effect for local treatment triggers systemic antitumor responses, ACS Nano 16 (2) (2022) 3070–3080.

[39] H.N. Bhatti, M. Madeeha, M. Asgher, N. Batool, Purification and thermodynamic characterization of glucose oxidase from a newly isolated strain ofAspergillus Niger, Can. J. Microbiol. 52 (6) (2006) 519–524.
[40] L. Zhi, Y. Jiang, Y. Wang, M. Hu, S. Li, Y. Ma, Effects of additives on the thermostability of chloroperoxidase, Biotechnol. Prog. 23 (3) (2008) 729–733.
[41] M.H. Chua, K.L.O. Chin, X.J. Loh, Q. Zhu, J. Xu, Aggregation-induced emission-active nanostructures: beyond biomedical applications, ACS Nano 17 (3) (2023) 1845–1878.
[42] H. Wang, Q. Li, P. Alam, H. Bai, V. Bhalla, M.R. Bryce, M. Cao, C. Chen, S. Chen, X. Chen, Y. Chen, Z. Chen, D. Dang, D. Ding, S. Ding, Y. Duo, M. Gao, W. He, X. He, X. Hong, Y. Hong, J.J. Hu, R. Hu, X. Huang, T.D. James, X. Jiang, G.I. Konishi, R.T. K. Kwok, J.W.Y. Lam, C. Li, H. Li, K. Li, N. Li, W.J. Li, Y. Li, X.J. Liang, Y. Liang, B. Liu, G. Liu, X. Liu, X. Lou, X.Y. Lou, L. Luo, P.R. McGonigal, Z.W. Mao, G. Niu, T. C. Owyong, A. Pucci, J. Qian, A. Qin, Z. Qiu, A.L. Rogach, B. Situ, K. Tanaka, Y. Tang, B. Wang, D. Wang, J. Wang, W. Wang, W.X. Wang, W.J. Wang, X. Wang, Y.F. Wang, S. Wu, Y. Wu, Y. Xiong, R. Xu, C. Yan, S. Yan, H.B. Yang, L.L. Yang, M. Yang, Y.W. Yang, J. Yoon, S.Q. Zang, J. Zhang, P. Zhang, T. Zhang, X. Zhang, X. Zhang, N. Zhao, Z. Zhao, J. Zheng, L. Zheng, Z. Zheng, M.Q. Zhu, W.H. Zhu, H. Zou, B.Z. Tang, Aggregation-induced emission (AIE), life and health, ACS Nano 17 (15) (2023) 14347–14405.
[43] A.H. Ashoka, I.O. Aparin, A. Reisch, A.S. Klymchenko, Brightness of fluorescent organic nanomaterials, Chem. Soc. Rev. 52 (14) (2023) 4525–4548.
[44] X. Li, T. Yong, Z. Wei, N. Bie, X. Zhang, G. Zhan, J. Li, J. Qin, J. Yu, B. Zhang, L. Gan, X. Yang, Reversing insufficient photothermal therapy-induced tumor relapse and metastasis by regulating cancer-associated fibroblasts, Nat. Commun. 13 (1) (2022) 2794.
[45] Y. Zhang, N. Pang, X. Huang, W. Meng, L. Meng, B. Zhang, Z. Jiang, J. Zhang, Z. Yi, Z. Luo, Z. Wang, L. Niu, Ultrasound deep brain stimulation decelerates telomere shortening in Alzheimer's disease and aging mice, Fundamental Research 3 (3) (2023) 469–478.
[46] C. Zhao, Y. Cheng, P. Huang, C. Wang, W. Wang, M. Wang, W. Shan, H. Deng, X-ray-Guided in situ genetic engineering of macrophages for sustained cancer immunotherapy, Adv. Mater. 35 (14) (2023) 2208059.
[47] F. Ruan, H. Fang, F. Chen, X. Xie, M. He, R. Wang, J. Lu, Z. Wu, J. Liu, F. Guo, W. Sun, D. Shao, Leveraging radiation-triggered metal prodrug activation through nanosurface energy transfer for directed radio-chemo-immunotherapy, Angew. Chem., Int. Ed. Engl. 63 (10) (2024) 202317943.
[48] Z. Wang, F. Chen, Y. Cao, F. Zhang, L. Sun, C. Yang, X. Xie, Z. Wu, M. Sun, F. Ma, D. Shao, K.W. Leong, R. Pei, An engineered nanoplatform with tropism toward irradiated glioblastoma augments its radioimmunotherapy efficacy, Adv. Mater. 36 (32) (2024) 2314197.